Materials Today Bio 32 (2025) 101688

Contents lists available at ScienceDirect

Materials Today Bio

journal homepage: www.journals.elsevier.com/materials-today-bio

Inherently anti-metastatic peptide hydrogels for sonodynamic-amplified ferroptosis in cancer therapy

Hongxia Zhang [a], Yamei Wang [b], Mengmeng Jiang [a], Kunyu Wang [a], Jingru Yan [a], Gongyu Li [b], Zhen Zheng [a,*]

[a] The Province and Ministry Co-sponsored Collaborative Innovation Center for Medical Epigenetics, Tianjin Key Laboratory on Technologies Enabling Development of Clinical Therapeutics and Diagnostics, School of Pharmacy, Tianjin Medical University, Tianjin, 300070, China

[b] Tianjin Key Laboratory of Biosensing and Molecular Recognition, Research Center for Analytical Science, Frontiers Science Center for New Organic Matter, College of Chemistry, Nankai University, Tianjin, 300071, China

ARTICLE INFO

Keywords:
Supramolecular hydrogel
Anti-metastasis
Self-assembly peptide
Sonodynamic therapy
Ferroptosis

ABSTRACT

Cancer metastasis remains a significant challenge in oncology, prompting the exploration of innovative biomaterials to enhance treatment efficacy. While many hydrogels only serve as passive carriers, this study presents two novel self-assembling peptides, **CWEWTWY** and **NapFFSGP**, which form supramolecular hydrogels with intrinsic anti-metastatic properties. We demonstrate a correlation between the nanofibrous morphology of these peptides and their enhanced anti-metastatic activity, mediated by disruption of F-actin organization and impacting pathways related to cancer cell adhesion and actin filament dynamics. *In vivo* studies confirm a significant reduction in lung metastasis using a 4T1 pulmonary metastasis model. We also demonstrate their potential as a simple, synergistic platform integrating sonodynamic therapy (SDT) and ferroptosis. Ironporphyrin (FP), incorporated into **Gel@FP**, acts as both a sonosensitizer and ferroptosis inducer. Upon ultrasound irradiation, FP generates localized reactive oxygen species, further amplifying ferroptosis through enhanced lipid peroxidation. **Gel@FP** combined with ultrasound demonstrates potent antitumor efficacy *in vitro* and *in vivo*, promoting apoptosis, ferroptosis, and immunogenic cell death, leading to enhanced tumor regression and robust immune activation. Our findings highlight the potential of anti-metastatic hydrogels as a promising multifunctional platform to address the challenges of metastasis while enhancing antitumor immunity.

1. Introduction

Cancer metastasis is a formidable challenge in oncology, contributing to the majority of cancer-related fatalities [1–4]. Traditional therapies often struggle to effectively manage metastatic cancer, necessitating the exploration of innovative biomaterials to enhance current treatment modalities and curtail metastatic progression [5–7]. Recent research has underscored the potential of nanofiber formation in impeding cancer cell migration and metastasis by disrupting F-actin polymerization, rearrangement, and cancer cell-extracellular matrix interactions [8–10]. Supramolecular hydrogels, comprised of self-assembled nanofibers, represent a promising approach in the biomaterials field for countering cancer metastasis [11–13]. These hydrogels' 3D networks function as physical barriers, restricting tumor cell mobility and invasive potential [14–16]. Despite extensive investigation into the localized delivery capabilities of supramolecular hydrogels, their potential as intrinsically anti-metastatic agents remain largely unexplored.

Sonodynamic therapy (SDT) is a non-invasive treatment modality that employs ultrasound waves to activate sonosensitizers, resulting in reactive oxygen species (ROS) generation and subsequent cancer cell apoptosis [17–19]. SDT's ability to penetrate deep into tissues and generate localized ROS makes it an attractive therapeutic strategy [20,21]. However, its effectiveness in inducing tumor apoptosis is constrained by cancer cells' inherent or acquired apoptosis resistance [22,23]. Therefore, exploring non-apoptotic pathways offers new opportunities for eliminating cancer cells and reducing the survival of apoptosis-resistant clones [24,25]. Ferroptosis, a non-apoptotic form of regulated cell death, is characterized by lipid peroxide accumulation and iron-dependent oxidative stress, stemming from dysregulated cellular metabolism and redox homeostasis [26–28]. Unlike apoptosis, which cancer cells often evade, ferroptosis presents a unique

* Corresponding author.
E-mail address: zhengzhen90@tmu.edu.cn (Z. Zheng).

https://doi.org/10.1016/j.mtbio.2025.101688
Received 13 January 2025; Received in revised form 28 February 2025; Accepted 19 March 2025
Available online 20 March 2025

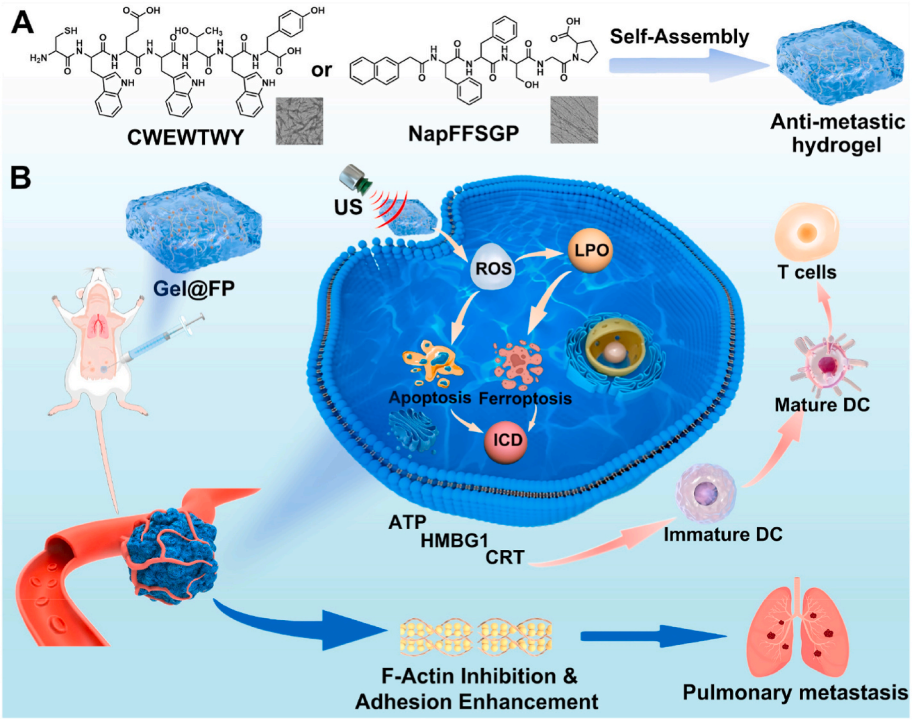

Scheme 1. (A) Chemical structures of the self-assembling peptides used to form the hydrogels. (B) Proposed mechanism of action for the anti-tumor and anti-metastatic activity of **Gel@FP**.

opportunity to bypass resistance mechanisms and selectively target cancer cells [29–32]. Therefore, the complementary mechanisms of SDT and ferroptosis provide a rationale for combining these therapies to achieve enhanced therapeutic outcomes [33–36]. However, current strategies to combine sonodynamic therapy (SDT) and ferroptosis often involve complex, multi-component systems, requiring separate delivery vehicles or multiple agents.

In this study, we identified two novel self-assembling peptides, **CWEWTWY** (Cys-Trp-Glu-Trp-Thr-Trp-Tyr), and **NapFFSGP** (Nap-Phe-Phe-Ser-Gly-Pro), capable of forming supramolecular hydrogels with inherent anti-metastatic properties (see Scheme 1). We establish a correlation between the nanofibrous morphology of these peptides and their enhanced anti-metastatic activity, mediated by disruption of F-actin organization and impacting pathways related to cell adhesion and actin filament dynamics. *In vivo* studies confirm a significant reduction in lung metastasis using a 4T1 pulmonary metastasis model. Focusing on the **NapFFSGP** hydrogel (**Gel Nap**), we demonstrate its potential as a simple, synergistic platform integrating SDT and ferroptosis. Iron-porphyrin (FP), incorporated into **Gel Nap** (**Gel@FP**), acts as both a sonosensitizer and ferroptosis inducer. Upon ultrasound irradiation, FP generates localized reactive oxygen species (ROS), further amplifying ferroptosis through enhanced lipid peroxidation. **Gel@FP** combined with ultrasound demonstrates potent antitumor efficacy *in vitro* and *in vivo*, promoting apoptosis, ferroptosis, and immunogenic cell death, leading to enhanced tumor regression and robust immune activation. Unlike conventional hydrogels that act solely as passive carriers for chemotherapeutics, our hydrogel exhibits intrinsic anti-metastatic activity by disrupting tumor cell migration pathways. This bioactivity persists even after drug loading, eliminating the need for exogenous anti-metastatic drugs. These anti-metastatic hydrogels offer a promising multifunctional strategy for preventing cancer spread and improving treatment outcomes.

2. Materials and methods

2.1. Peptide synthesis and characterization

Peptides **Fmoc FF** (Fmoc-Phe-Phe), **CWEWTWY** (Cys-Trp-Glu-Trp-Thr-Trp-Tyr), and **NapFFSGP** (Nap-Phe-Phe-Ser-Gly-Pro) were synthesized using standard Fmoc solid-phase peptide synthesis (SPPS). Crude peptides were purified using high-performance liquid chromatography (HPLC), and their purity was confirmed via HPLC and high-resolution mass spectrometry (HRMS).

2.2. Hydrogel preparation

CWEWTWY and **NapFFSGP** peptide (2 mg) was dissolved in 200 μL of 0.2 M phosphate buffer (PB, pH 6.5) and sonicated for 15 min to ensure complete dispersion. The mixture was incubated at room temperature for 6 h to allow for hydrogel formation. The two hydrogels formed are referred to as "**Gel CW**" and "**Gel Nap**".

2.3. In vivo anti-metastatic studies

All animal experiments were approved by the Animals Experimentation Ethics Committee of Tianjin Medical University (No. TMUa-MEC2023008) and conducted according to institutional guidelines. Female BALB/c mice were injected with luciferase-expressing 4T1 cells (5×10^4 cells in 50 μL) via the tail vein to establish a pulmonary metastasis model. Three days post-injection, mice received daily intraperitoneal injections of PBS, **Gel CW**, or **Gel Nap** (1.0 wt%). Tumor growth was monitored every 3–4 days using whole-body bioluminescence imaging. On day 9, mice were sacrificed, and lung tissues were collected for analysis by Indian Ink and H&E staining.

2.4. Hydrogel *Gel@FP* characterization

Gel@FP Preparation: Ironporphyrin (FP) was dissolved in DMSO to prepare a stock solution. **NapFFSGP** peptide was then dissolved in PB

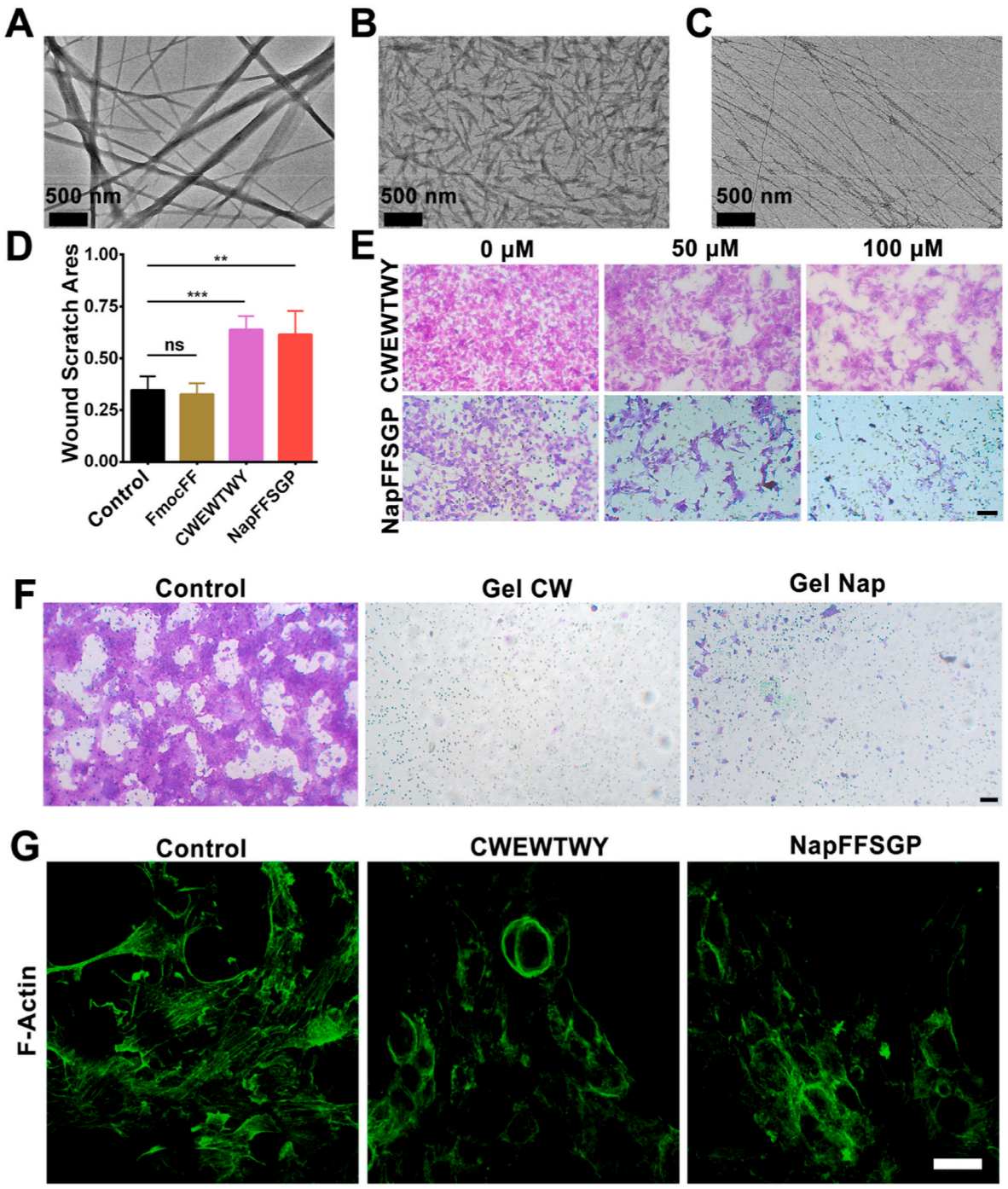

Fig. 1. *In vitro* anti-metastatic activity. TEM images of (A) **FmocFF**, (B) **CWEWTWY**, and (C) **NapFFSGP**. Scale bar: 500 nm. (D) The quantification of the wound scratch area in 4T1 tumor cells. Transwell invasion assays of 4T1 cells treated with (E) **CWEWTWY**, and **NapFFSGP** (0, 50, and 100 μM) and (F) **Gel CW** and **Gel Nap**. Scale bar: 100 μm. (G) Effects of different treatments on tumor cell F-actin. Scale bar: 20 μm.

containing the desired concentration of FP (e.g., 50 μM). This mixture was sonicated and incubated as described above to obtain the drug-loaded hydrogel **Gel@FP**. Rheological properties of both **Gel Nap** and **Gel@FP** were assessed using a Discovery HR-20 TA rheometer.

2.5. Lipid peroxidation (LPO) detection in vitro

LPO was detected using the C11-BODIPY 581/591 probe. 4T1 cells were seeded in 24-well plates and treated with PBS, FP + US (0.3 W/cm^2, 1.0 MHz, 1 min), **Gel@FP**, or **Gel@FP** + US (0.3 W/cm^2, 1.0 MHz, 1 min). After incubation with the C11-BODIPY581/591 probe for 1 h, cells were imaged using a fluorescence inverted microscope.

2.6. Immunofluorescence staining in vitro

4T1 cells (1×10^5 cells/well) in 24-well plates were treated with PBS, FP + US (0.3 W/cm^2, 1.0 MHz, 1 min), **Gel@FP**, or **Gel@FP** + US (0.3 W/cm^2, 1.0 MHz, 1 min). After 4 h, cells were fixed, permeabilized, and blocked with 10 % goat serum. Cells were then incubated with primary antibodies overnight at 4 °C, followed by incubation with FITC-labeled secondary antibodies for 2 h. After counterstaining with DAPI, images were acquired using fluorescence microscopy, and fluorescence

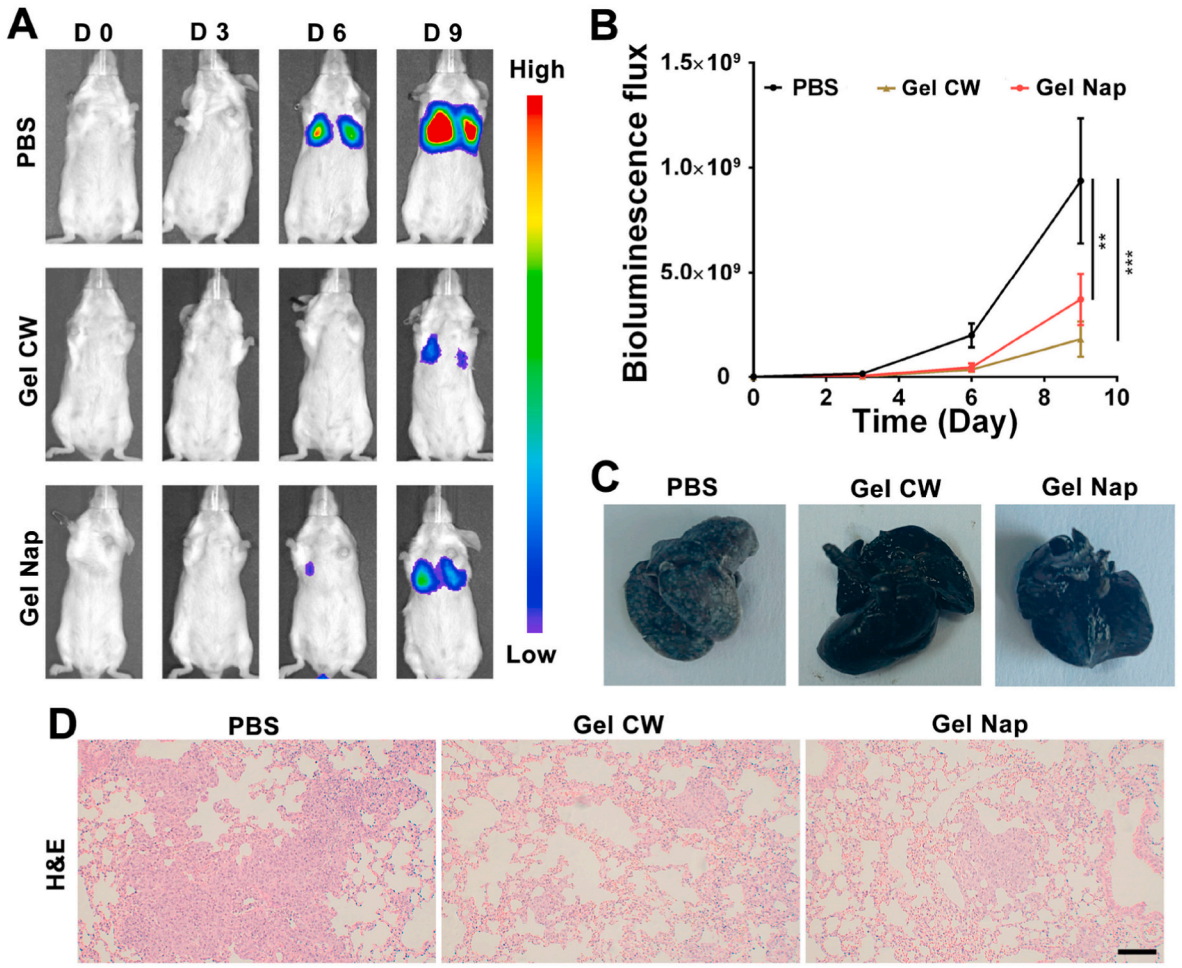

Fig. 2. *In vivo* anti-metastatic activity. (A) Representative *in vivo* bioluminescent images. (B) Quantification of total bioluminescence flux in mice with different treatments. (C) Photographs of lung metastases harvested on day 9. (D) H&E-stained images of lung tissue from different treatments. Scale bar: 100 μm $^{**}p < 0.01$, $^{***}p < 0.001$.

intensity was quantified using ImageJ.

2.7. In vitro cytotoxicity assay

4T1 cells were seeded in 96-well plates and treated with varying concentrations of **Gel CW**, **Gel Nap**, FP or **Gel@FP** (equivalent FP concentration: 1–25 μM) for 24 h. Cells were then irradiated with US (1.0 W/cm^2, 1.0 MHz, 5 min) or left untreated and incubated for an additional 24 h. Cell viability was determined using the MTT assay. To visualize cytotoxicity, cells were stained with calcein AM and propidium iodide (PI) and imaged.

2.8. In vivo antitumor study

Once tumors reached approximately 50 mm^3, 4T1 tumor-bearing BALB/c mice were randomly divided into six groups: (i) PBS, (ii) **Gel Nap**, (iii) FP (2.5 mg/kg), (iv) FP + US, (v) **Gel@FP** (equivalent to a FP dose of 2.5 mg/kg), and (vi) **Gel@FP** + US. Mice received peritumoral injections (50 μL) of the assigned treatment every two days for a total of three treatments. Two hours post-injection, US-treated groups received US irradiation (1.0 W/cm^2, 1.0 MHz, 5 min). Body weight and tumor volume were measured every two days. At the end of the study, mice were sacrificed, and tumors and spleens were collected for histological analysis (H&E, TUNEL, PRDX3, and CD8 staining) and flow cytometry, respectively.

3. Results and discussion

3.1. Nanostructure morphology and in vitro anti-metastatic activity

To investigate the impact of peptide sequence and self-assembly morphology on anti-metastatic activity, three peptides with varying amino acid sequences and lengths—**FmocFF**, **NapFFSGP**, and **CWEWTWY** were synthesized via solid-phase peptide synthesis (SPPS). Following purification by HPLC, peptide structures were confirmed using HRMS (Figs. S1–S3). Transmission electron microscopy (TEM) analysis revealed distinct nanostructures formed by each peptide. **FmocFF** self-assembled into uniform nanobelts with an average diameter of 55.6 ± 7 nm (Fig. 1A). In contrast, **CWEWTWY** formed short, needle-like nanofibers with average diameters of 23.4 ± 2 nm, while **NapFFSGP** assembled into long nanofibers with average diameters of 10.9 ± 0.8 nm (Fig. 1B and C). Circular dichroism (CD) spectroscopy was employed to characterize the secondary structures of the self-assembled peptides (Fig. S4). **FmocFF** and **CWEWTWY** exhibited a mixture of α-helix (35 % and 40 %, respectively), β-turn (23 % and 24 %, respectively), and random coil (32 % and 38 %, respectively) structures. The observed secondary structure, characterized by a high α-helical content along with a high proportion of β-turns, was consistent with previously reported structures [37–39]. In contrast, **NapFFSGP** predominantly adopted a β-sheet conformation (49 %), with contributions from β-turn (23 %) and random coil (25 %) structures. These structural variations likely arise from differences in amino acid sequence, length,

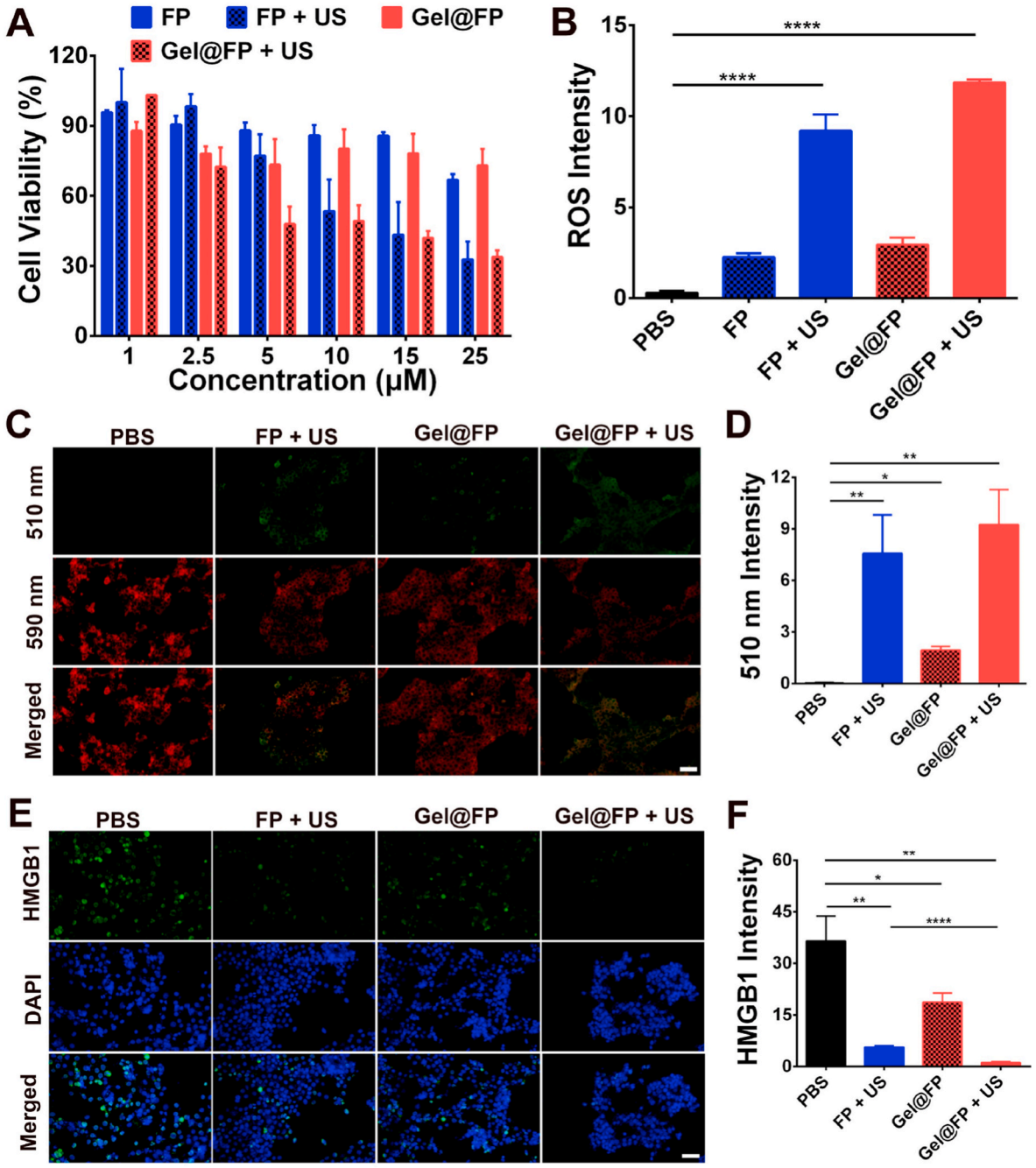

Fig. 3. *In vitro* antitumor efficacy and mechanism of cell death. (A) Cytotoxicity of FP and **Gel@FP** against 4T1 tumor cells with or without US irradiation. (B) Semi-quantification of intracellular DCFH fluorescence intensity. (C) Intracellular LPO accumulation in 4T1 tumor cells after treatment with PBS, FP + US, **Gel@FP**, and **Gel@FP** + US. (D) Quantitative data of the fluorescence intensity of 510 nm channel in the immunofluorescence images. (E) HMGB1 levels in 4T1 cells after different treatments. (F) Quantitative data of the fluorescence intensity of HMGB1 in the immunofluorescence images. Scale bar: 100 μm $^{*}p < 0.05$, $^{**}p < 0.01$, $^{****}p < 0.0001$.

and N-terminal capping groups, influencing intermolecular interactions such as π−π stacking and hydrogen bonding.

Building on previous studies demonstrating the inhibitory effects of self-assembling nanofibers on cancer cell migration and invasion, we evaluated the anti-metastatic potential of these peptides [40]. A wound healing assay revealed negligible inhibition of wound closure in both the PBS and **FmocFF**-treated groups (Fig. S5 and Fig. 1D). Conversely, treatment with **CWEWTWY** and **NapFFSGP** significantly reduced wound healing, suggesting that longer peptide sequences forming nanofibrous structures exhibit greater inhibitory effects on tumor cell migration. To further evaluate the anti-invasive potential of **CWEWTWY** and **NapFFSGP**, a transwell assay was conducted. Both peptides demonstrated potent anti-invasive activity against 4T1 cells compared to the PBS control (Fig. 1E). We further investigated the impact of hydrogel formulation on the peptides' ability to inhibit cell migration (Figs. S6 and S7) and invasion (Fig. 1F). Both **Gel CW** and **Gel Nap** exhibited enhanced inhibitory effects compared to their respective peptide solutions (**CWEWTWY** and **NapFFSGP**), demonstrating the improved efficacy of hydrogel formation.

To investigate the underlying mechanism of the observed anti-metastatic effects, we examined F-actin filament organization, a key regulator of cell motility and invasion, using phalloidin staining. As

depicted in Fig. 1G, PBS-treated 4T1 cells displayed normal, elongated F-actin filaments. In contrast, treatment with **CWEWTWY** or **NapFFSGP** led to disrupted and shortened F-actin microfilaments. This disruption suggests that these peptides exert their anti-metastatic activity by directly or indirectly interfering with F-actin polymerization and organization, thereby impeding cell motility and invasive capacity.

3.2. In vivo anti-metastatic activity

To evaluate the *in vivo* anti-metastatic efficacy of **CWEWTWY** and **NapFFSGP**, we utilized an aggressive 4T1 pulmonary metastasis model in luciferase-transfected mice. Tumor growth and metastasis were monitored every three days using an IVIS imaging system. Notably, both **CWEWTWY** and **NapFFSGP** treatments significantly impeded lung metastasis compared to the PBS control group (Fig. 2A). Quantification of total luminescence signals within the lung region confirmed these observations, revealing a substantial reduction in luminescence intensity 5.18-fold for **CWEWTWY** and 2.54-fold for **NapFFSGP** compared to PBS-treated mice on day 9 (Fig. 2B).

Following sacrifice on day 9, lung tissues were collected and stained with Indian Ink to visualize macroscopic metastatic nodules. Consistent with the IVIS imaging data, both **CWEWTWY** and **NapFFSGP** treatments resulted in a significant reduction in the number of pulmonary nodules compared to the PBS group (Fig. 2C). Quantitative analysis revealed a substantial difference in metastatic burden between treated and untreated lungs. As shown in Fig. S8, the untreated lungs averaged around 200 diffusely distributed nodules, while lungs treated with **Gel CW** or **Gel Nap** averaged fewer than 30 nodules. Histological analysis using hematoxylin and eosin (H&E) staining further supported these findings (Fig. 2D). Importantly, no significant changes in body weight or pathological abnormalities were observed in peptide-treated mice, indicating good biocompatibility of the peptides *in vivo* (Fig. S9). These results highlight the potential of designing self-assembling peptide-based hydrogels as a novel strategy for combating cancer metastasis.

3.3. Characterization and sonodynamic properties of *Gel@FP*

In addition to their promising anti-metastatic activities, both **CWEWTWY** and **NapFFSGP** exhibited the capacity to self-assemble into supramolecular hydrogels. **NapFFSGP** was selected for further investigation and development due to its ability to undergo facile hydrogelation upon sonication. To explore its potential in SDT, the sonosensitizer FP was loaded into the **NapFFSGP** hydrogel matrix, yielding **Gel@FP** (Fig. S10A). Scanning transmission electron microscopy (STEM) coupled with energy-dispersive X-ray spectroscopy (EDX) elemental mapping was performed on the **Gel@FP** sample. The resulting elemental maps (Fig. S10B) reveal a uniform distribution of iron, confirming the successful incorporation and distribution of FP within the hydrogel. Furthermore, the loading efficiency was determined to be 97.5 % ± 2.7 %.

The physicochemical properties of the resulting hydrogel were then characterized both before and after FP encapsulation. Rheological analysis of Gel revealed higher storage moduli (G′) than loss moduli (G″) over a frequency range of 0.1–10 Hz and a strain range of 0.1–10 %, confirming the formation of a stable hydrogel (Figs. S11A and S11B). Importantly, the loading of FP within the hydrogel did not significantly alter the hydrogel's viscoelastic properties (Figs. S11C and S11D).

We next investigated the sonodynamic properties of both free and hydrogel-encapsulated FP (**Gel@FP**). **Gel@FP** efficiently generated hydroxyl radicals (•OH) via the Fenton reaction [41], as evidenced by continuous methylene blue degradation in the presence of H_2O_2 under acidic conditions (Fig. S12). Further demonstrating its sonodynamic potential, FP exhibited a 12-fold increase in ROS generation in PBS compared to DMSO upon ultrasound irradiation (Fig. S13), and both free FP and **Gel@FP** showed superior sonosensitizing capabilities compared to Ce6 [42], as indicated by time-dependent increases in 2′,7′-dichlorofluorescein diacetate (DCFH) fluorescence intensity (Figs. S14A–D). Finally, **Gel@FP** + US treatment caused the most pronounced reduction in 1,3-diphenylisobenzofuran (DPBF) absorbance [43], indicating efficient singlet oxygen ($^1O_2$) generation (Figs. S14E–H). These findings collectively demonstrate that **Gel@FP** acts as an effective sonosensitizer formulation without compromising the sonodynamic properties of FP.

3.4. Antitumor efficacy and mechanism of cell death in vitro

Having demonstrated the enhanced sonodynamic properties of FP within the **NapFFSGP** hydrogel, we next evaluated the *in vitro* therapeutic efficacy of **Gel@FP** against 4T1 cells. MTT assays demonstrated negligible cytotoxicity of both **Gel CW** and **Gel Nap** alone against 4T1 tumor cells. As shown in Fig. S15, cell viability remained above 90 % even at a concentration of 600 μM, indicating good biocompatibility of both hydrogels themselves. While both FP alone and **Gel@FP** alone resulted in moderate cytotoxicity (66.92 % and 73.10 % cell viability at 25 μM, respectively), US irradiation significantly enhanced their antitumor effects, reducing cell viability to 32.77 % and 33.86 % at 25 μM, respectively (Fig. 3A). Annexin V-FITC/PI staining confirmed increased induction of apoptosis following **Gel@FP** + US treatment compared to controls and individual treatments (Fig. S16).

To elucidate the mechanisms underlying the observed antitumor effects, we investigated ROS generation and the role of ferroptosis [44–46]. **Gel@FP** + US treatment resulted in robust intracellular ROS generation, as evidenced by strong DCFH-DA fluorescence (Figs. S17 and 3B). This was accompanied by increased lipid peroxidation (LPO), indicated by a pronounced fluorescence shift in the BODIPY-C11 probe (Fig. 3C and D, S18). Furthermore, we observed a decrease in intracellular glutathione (GSH) levels. While **Gel@FP** treatment alone induced a slight reduction in GSH (likely due to Fenton reactions), the combination of FP + US and **Gel@FP** + US resulted in more substantial GSH depletion, suggesting that ultrasound irradiation enhances ROS production and subsequent GSH consumption (Fig. S19). To confirm the occurrence of ferroptosis induced by **Gel@FP** + US treatment, we examined key ferroptosis markers by immunofluorescence. As illustrated in Fig. S20, the **Gel@FP** + US treatment significantly decreased the expression of glutathione peroxidase 4 (GPX4), a critical regulator that normally prevents ferroptosis by reducing lipid peroxides. Additionally, we observed increased expression of peroxiredoxin 3 (PRDX3) following treatment (Fig. S21). Together, these molecular changes—decreased GPX4 and increased PRDX3—provide strong evidence for the induction of ferroptosis as a mechanism of cell death in our treatment model.

Finally, to investigate the potential of **Gel@FP**-mediated SDT to induce immunogenic cell death (ICD), the levels of the damage-associated molecular patterns (DAMPs) high mobility group box-1 protein (HMGB1), calreticulin (CRT), and adenosine triphosphate (APT) were assessed [47]. Immunofluorescence was used to assess HMGB1 and CRT (Fig. 3E and F, S22), while an ATP assay kit was used to quantify ATP levels. **Gel@FP** + US treatment significantly decreased intracellular HMGB1 while increasing CRT exposure on the cell membrane. Importantly, the **Gel@FP** + US treatment also significantly increased extracellular ATP levels compared to the control groups (Fig. S23), providing further evidence of its ability to induce ICD. Our investigation demonstrates the significant therapeutic potential of **Gel@FP** combined with ultrasound irradiation against 4T1 cells. This synergistic treatment promotes apoptosis, triggers ferroptosis through robust ROS generation and lipid peroxidation, and enhances immunogenic cell death, highlighting its promise for cancer therapy.

3.5. In vivo antitumor efficacy and immune activation

Following the promising *in vitro* results, the *in vivo* antitumor efficacy of **Gel@FP** was evaluated in a 4T1 tumor-bearing mouse model. Mice were randomly assigned to six groups: (i) PBS, (ii) **Gel Nap**, (iii) FP, (iv)

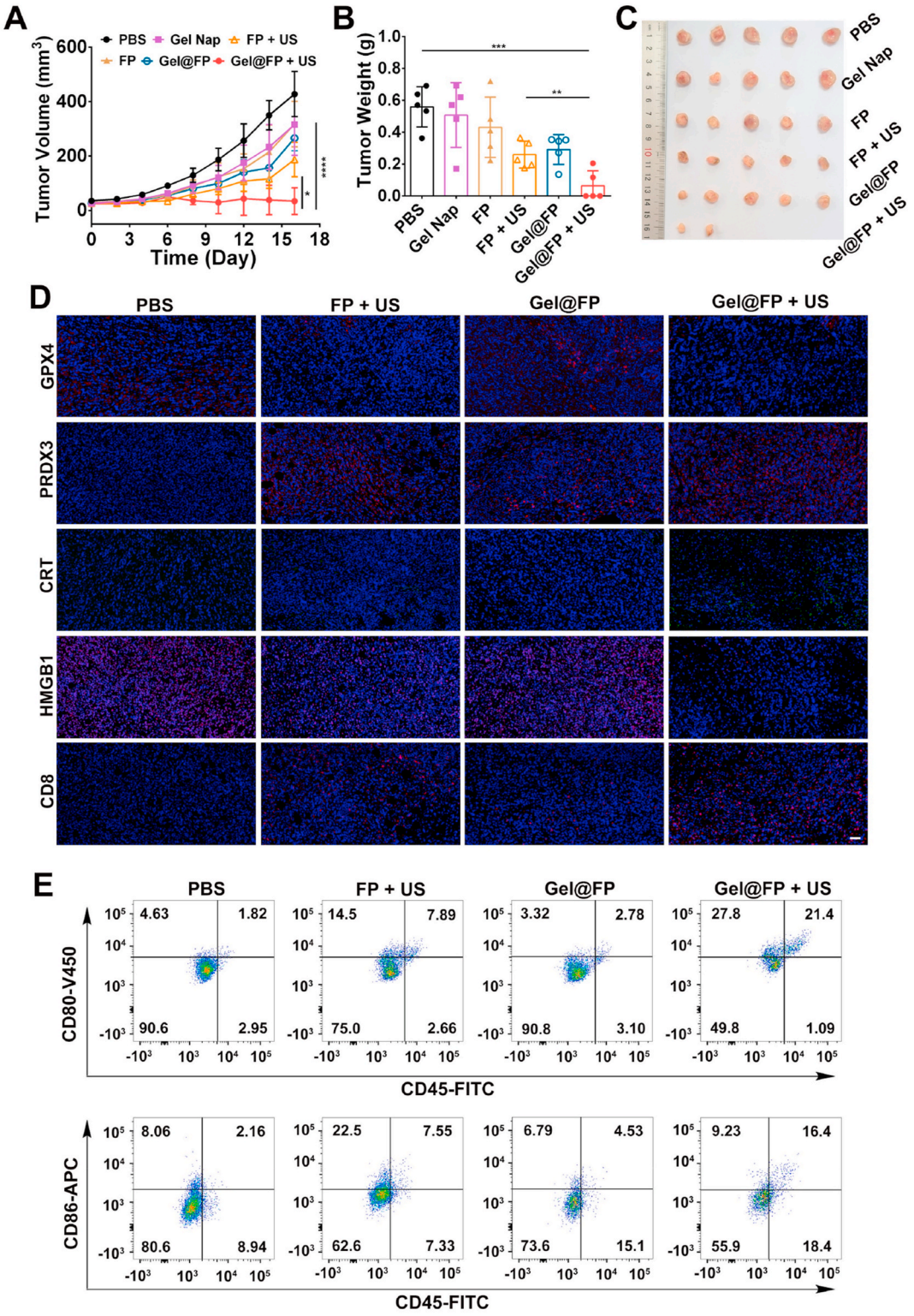

Fig. 4. *In vivo* antitumor efficacy and immune activation. (A) Tumor growth curves of mice treated with different formulations. (B) Tumor weights on day 16. (C) Representative tumor photographs of 4T1 tumor-bearing mice at 16 days post-treatment. (D) Immunofluorescence staining of GPX4, PRDX3, CRT, HMGB1, and CD8 in tumor tissues. (E) Flow cytometry analysis of DC maturation markers in the spleen. Scale bars: 100 μm ****$p < 0.0001$.

FP + US, (v) **Gel@FP**, and (vi) **Gel@FP** + US. US-involved groups received irradiation at 1.0 W/cm^2, 1 MHz for 5 min. As shown in Fig. 4A, **Gel@FP** + US treatment resulted in the most significant tumor growth inhibition throughout the treatment period. By day 16, the average tumor weight in the **Gel@FP** + US group was only 11.5 % of that in the PBS control group (Fig. 4B and C). Histological analysis of tumor tissues using hematoxylin and eosin (H&E) and TUNEL staining revealed extensive karyolysis, cellular fragmentation, and apoptosis in the **Gel@FP** + US group (Figs. S24A and S24B). To further confirm the mechanism of cell death *in vivo*, we performed immunofluorescence staining of key ferroptosis markers in tumor tissues. As shown in Fig. 4D and Fig. S24B, tumors treated with **Gel@FP** + US exhibited significantly

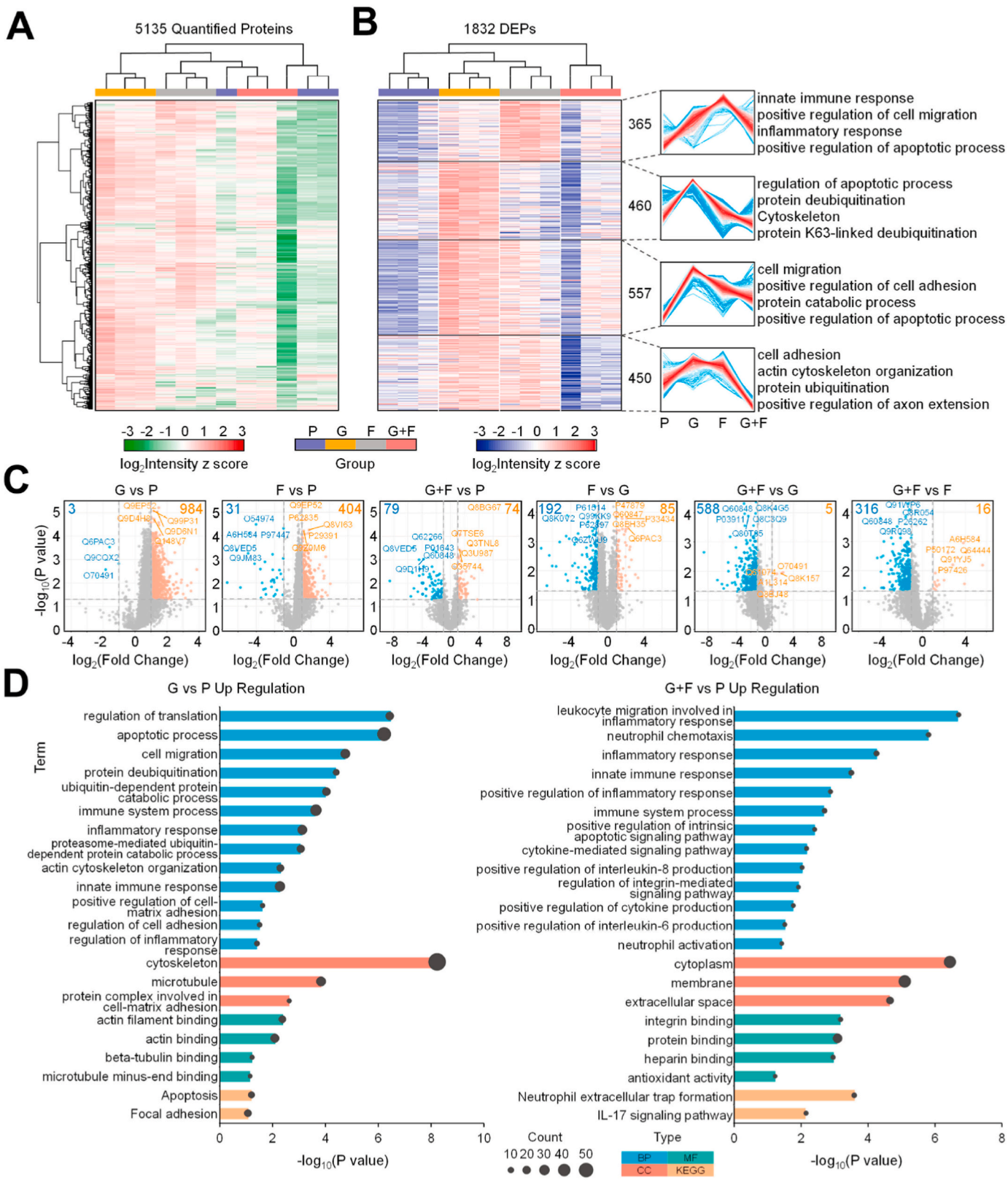

Fig. 5. Proteomics analysis of tumor tissues. (A) Hierarchical clustering of 5135 quantified proteins from tumor tissues. (P: PBS, G: **Gel Nap**, F: FP + US, G + F: **Gel@FP** + US). (B) Hierarchical clustering of 1832 significantly changed proteins based on ion intensities. The number of proteins within each cluster and selected enriched biological processes/pathways are indicated. (C) Volcano plots depicting pairwise comparisons of protein expression levels between different treatment groups. Significantly altered proteins (two-sided *t*-test, p-value <0.05, adjusted for multiple comparisons using the Benjamini-Hochberg method, fold change >2) are shown above the horizontal dashed line. Blue dots represent downregulated proteins, and orange dots represent upregulated proteins. (D) Gene Ontology (GO) enrichment and Kyoto Encyclopedia of Genes and Genomes (KEGG) pathway analysis of differentially expressed proteins.

decreased expression of GPX4 alongside markedly upregulated PRDX3 levels. These molecular changes mirror our *in vitro* findings and provide compelling evidence that ferroptosis is a primary cell death mechanism induced by **Gel@FP** + US treatment *in vivo*.

The ability of **Gel@FP** + US to induce ICD was also evaluated *in vivo*. Tumor tissues were analyzed via immunofluorescence staining for ICD hallmarks. As shown in Fig. 4D and Fig. S24B, the **Gel@FP** + US group exhibited the most pronounced CRT exposure, with fluorescence intensity 1.5-fold higher than the FP + US group and 3-fold higher than the **Gel@FP** group, confirming ultrasound-triggered amplification of CRT membrane translocation. Furthermore, HMGB1 showed the most significant cytoplasmic translocation in the **Gel@FP** + US cohort. This coordinated upregulation of CRT and HMGB1 release provides direct evidence of robust ICD activation *in vivo*. To assess immune activation, tumor tissues were stained for $CD8^+$ T cells. **Gel@FP** + US treatment led to the highest level of $CD8^+$ T cell infiltration, suggesting a potent antitumor immune response (Fig. 4D, S24B). Flow cytometry analysis of splenic dendritic cells (DCs) revealed that **Gel@FP** + US treatment significantly increased the expression of the maturation markers CD45, CD80, and CD86 (Fig. 4E). Furthermore, **Gel@FP** + US treatment resulted in the highest frequency of $CD8^+$ T cells in the spleen, indicating systemic immune activation (Fig. S24C). Importantly, **Gel@FP** treatment did not induce significant changes in body weight or histopathological abnormalities in major organs, suggesting a favorable safety profile *in vivo* (Fig. S25). These findings highlight the potential of **Gel@FP** + US as a safe and effective therapeutic strategy for cancer treatment.

3.6. Mechanistic insights into metastasis inhibition in vivo

To elucidate the mechanisms underlying the observed metastasis inhibition, we performed a comprehensive proteomic analysis of tumor tissues from different treatment groups. Hierarchical clustering of all quantified proteins revealed distinct protein profiles across treatments, with greater intergroup differences compared to intragroup variations (Fig. 5A). This finding suggests that each treatment modality induced unique proteomic alterations within the tumor microenvironment.

To identify differentially expressed proteins (DEPs) between treatment groups, we performed pairwise comparisons using Student's t-test (p-value <0.05, fold change >2). Hierarchical clustering of these DEPs further emphasized the distinct proteomic signatures associated with each treatment, resulting in four well-defined clusters (Fig. 5B). Volcano plots visually represent the DEPs, highlighting proteins with significant abundance changes (Fig. 5C). Gene Set Variation Analysis (GSVA) was employed to explore the functional implications of the observed proteomic changes. GSVA revealed significant enrichment of specific cellular components, biological processes, molecular functions, and pathways within each cluster. Notably, the **Gel Nap** group exhibited a striking enrichment in pathways directly related to cell adhesion, actin filament binding, and actin binding dynamics, as evidenced by the proteomic analysis (Fig. 5D). This finding provides compelling evidence to suggest that **Gel Nap**'s potent metastasis-inhibiting effects are mediated, at least partially, through its influence on these crucial cellular processes. The upregulation of proteins involved in cell adhesion suggests that **Gel Nap** may promote the attachment of tumor cells to the extracellular matrix or neighboring cells. This increased adhesion could physically restrain tumor cells, preventing them from detaching from the primary tumor mass and initiating the metastatic cascade. Moreover, the observed enrichment in pathways related to actin filament binding and dynamics indicates that **Gel Nap** likely influences the organization and polymerization of actin filaments within tumor cells, consistent with our cell experiment findings. This modulation could disrupt the formation of lamellipodia and filopodia, structures that are essential for cell migration and invasion. These findings highlight the multifaceted mechanisms by which **Gel Nap** exerts its anti-metastatic effects.

Interestingly, the **Gel@FP** + US group displayed upregulation of pathways associated with inflammatory and innate immune responses. This observation suggests that the combination of SDT and ferroptosis induction via **Gel Nap** may trigger a systemic innate immune response, potentially contributing to the enhanced therapeutic efficacy observed with this combinatorial approach.

4. Conclusion

In conclusion, this study demonstrates the potent anti-metastatic and antitumor efficacy of self-assembling peptide-based hydrogels and their sonodynamically active formulation with the sonosensitizer FP. Our findings reveal a correlation between the nanofibrous morphology of these self-assembling peptides and their enhanced anti-metastatic activity *in vitro*, likely mediated by disruption of F-actin organization. This disruption impairs cancer cell migration and invasion, effectively limiting metastatic potential. *In vivo* studies using a 4T1 pulmonary metastasis model corroborated these findings, demonstrating a substantial reduction in lung metastasis following treatment with both **CWEWTWY** and **NapFFSGP**. Furthermore, proteomic analysis revealed that **Gel Nap** significantly impacts pathways related to cell adhesion and actin filament dynamics, providing mechanistic insights into its metastasis-inhibiting properties.

Emerging strategies for anti-metastatic treatment include angiogenesis inhibitors (e.g., bevacizumab), cytotoxic chemotherapeutics (e.g., doxorubicin), and immune checkpoint inhibitors (e.g., pembrolizumab). These approaches, while often effective, can be associated with significant systemic toxicities, development of drug resistance, and high costs. Our injectable hydrogel system offers a distinct advantage by exhibiting intrinsic anti-metastatic activity through the disruption of tumor cell migration pathways. Furthermore, its dual functionality as both a therapeutic agent and a drug delivery system potentially reduces the need for exogenous anti-metastatic drugs, thereby minimizing off-target effects. While our current system relies on passive diffusion for payload release, which may limit its efficacy in certain scenarios, it provides a foundation for future development of stimuli-responsive release mechanisms triggered by the tumor microenvironment (e.g., pH, enzymes). Such advancements could further enhance the targeted delivery and therapeutic efficacy of the hydrogel system, offering a potentially safer and more effective approach to combating metastasis compared to existing treatments.

CRediT authorship contribution statement

Hongxia Zhang: Writing – original draft, Software, Formal analysis. **Yamei Wang:** Visualization, Software. **Mengmeng Jiang:** Visualization. **Kunyu Wang:** Visualization. **Jingru Yan:** Visualization. **Gongyu Li:** Resources, Project administration. **Zhen Zheng:** Writing – review & editing, Resources, Project administration, Methodology, Funding acquisition.

Declaration of competing interest

The authors declare that they have no known competing financial interests or personal relationships that could have appeared to influence the work reported in this paper.

Acknowledgments

This work was supported by the Young Scientific and Technological Talents in Tianjin (J0700204), the Natural Science Foundation of Tianjin (24JCQNJC01050) and the National Natural Science Foundation of China (Grants 22204121 to ZZ; 22474062 to GL).

Appendix ASupplementary data

Supplementary data to this article can be found online at https://doi.

org/10.1016/j.mtbio.2025.101688.

Data availability

Data will be made available on request.

References

[1] S.U. Khan, K. Fatima, F. Malik, H. Kalkavan, A. Wani, Cancer metastasis: molecular mechanisms and clinical perspectives, Pharmacol. Ther. 250 (2023) 108522.
[2] C.L. Chaffer, R.A. Weinberg, A perspective on cancer cell metastasis, Science 331 (6024) (2011) 1559–1564.
[3] X. Guan, Cancer metastases: challenges and opportunities, Acta Pharm. Sin. B 5 (5) (2015) 402–418.
[4] M. Castaneda, P. den Hollander, N.A. Kuburich, J.M. Rosen, S.A. Mani, Mechanisms of cancer metastasis, Semin. Cancer Biol. 87 (2022) 17–31.
[5] J.M. Karp, R. Langer, Development and therapeutic applications of advanced biomaterials, Curr. Opin. Biotechnol. 18 (5) (2007) 454–459.
[6] Z. Jing, Q. Du, X. Zhang, Y. Zhang, Nanomedicines and nanomaterials for cancer therapy: progress, challenge and perspectives, Chem. Eng. J. 446 (2022) 137147.
[7] C. Wang, Y. Ye, Q. Hu, A. Bellotti, Z. Gu, Tailoring biomaterials for cancer immunotherapy: emerging trends and future outlook, Adv. Mater. 29 (29) (2017) 1606036.
[8] Z. Feng, H. Wang, F. Wang, Y. Oh, C. Berciu, Q. Cui, E.H. Egelman, B. Xu, Artificial intracellular filaments, Cell Rep. Phys. Sci. 1 (7) (2020) 100085.
[9] S.R. Roy, G. Li, X. Hu, S. Zhang, S. Yukawa, E. Du, Y. Zhang, Integrin and heparan sulfate dual-targeting peptide assembly suppresses cancer metastasis, ACS Appl. Mater. Interfaces 12 (17) (2020) 19277–19284.
[10] H. Wang, J. Wei, C. Yang, H. Zhao, D. Li, Z. Yin, Z. Yang, The inhibition of tumor growth and metastasis by self-assembled nanofibers of taxol, Biomaterials 33 (24) (2012) 5848–5853.
[11] S. Luo, J. Feng, L. Xiao, L. Guo, L. Deng, Z. Du, Y. Xue, X. Song, X. Sun, Z. Zhang, Y. Fu, T. Gong, Targeting self-assembly peptide for inhibiting breast tumor progression and metastasis, Biomaterials 249 (2020) 120055.
[12] J. Li, K. Shi, Z.F. Sabet, W. Fu, H. Zhou, S. Xu, T. Liu, M. You, M. Cao, M. Xu, X. Cui, B. Hu, Y. Liu, C. Chen, New power of self-assembling carbonic anhydrase inhibitor: short peptide-constructed nanofibers inspire hypoxic cancer therapy, Sci. Adv. 5 (9) (2019) eaax0937.
[13] C. Ren, Y. Gao, Y. Guan, Z. Wang, L. Yang, J. Gao, H. Fan, J. Liu, Carrier-free supramolecular hydrogel composed of dual drugs for conquering drug resistance, ACS Appl. Mater. Interfaces 11 (37) (2019) 33706–33715.
[14] Z. Balion, E. Sipailaite, G. Stasyte, A. Vailionyte, A. Mazetyte-Godiene, I. Seskeviciute, R. Bernotiene, J. Phopase, A. Jekabsone, Investigation of cancer cell migration and proliferation on synthetic extracellular matrix peptide hydrogels, Front. Bioeng. Biotechnol. 8 (2020) 773.
[15] Y. Ding, D. Zheng, L. Xie, X. Zhang, Z. Zhang, L. Wang, Z.-W. Hu, Z. Yang, Enzyme-instructed peptide assembly favored by preorganization for cancer cell membrane engineering, J. Am. Chem. Soc. 145 (8) (2023) 4366–4371.
[16] W. Zhang, S. Li, Y. Liu, R. Xing, Z. Jin, X. Yan, H. Xue, Immunosuppressive microenvironment improvement and treatment of aggressive malignancy pancreatic ductal adenocarcinoma based on local administration of injectable hydrogel, Nano Today 50 (2023) 101832.
[17] L. Jia, Y. Wang, T. Hu, C. Yang, H. Lin, F. Zhang, F. Qu, L. Cui, W. Guo, Boosting the tumor photothermal therapy with hollow CoSnSx-based injectable hydrogel via the sonodynamic and dual-gas therapy, Chem. Eng. J. 469 (2023) 143969.
[18] V. MiŠÍK, P. Riesz, Free radical intermediates in sonodynamic therapy, Ann. NY. Acad. Sci. 899 (1) (2000) 335–348.
[19] Z. Jiang, W. Xiao, Q. Fu, Stimuli responsive nanosonosensitizers for sonodynamic therapy, J. Contr. Release 361 (2023) 547–567.
[20] K.M. Nowak, M.R. Schwartz, V.R. Breza, R.J. Price, Sonodynamic therapy: rapid progress and new opportunities for non-invasive tumor cell killing with sound, Cancer Lett. 532 (2022) 215592.
[21] A. Ma, H. Chen, Y. Cui, Z. Luo, R. Liang, Z. Wu, Z. Chen, T. Yin, J. Ni, M. Zheng, L. Cai, Metalloporphyrin complex-based nanosonosensitizers for deep-tissue tumor theranostics by noninvasive sonodynamic therapy, Small 15 (5) (2019) 1804028.
[22] J. Li, Z. Yue, M. Tang, W. Wang, Y. Sun, T. Sun, C. Chen, Strategies to reverse hypoxic tumor microenvironment for enhanced sonodynamic therapy, Adv. Healthcare Mater. 13 (1) (2024) 2302028.
[23] J. Ouyang, Z. Tang, N. Farokhzad, N. Kong, N.Y. Kim, C. Feng, S. Blake, Y. Xiao, C. Liu, T. Xie, W. Tao, Ultrasound mediated therapy: recent progress and challenges in nanoscience, Nano Today 35 (2020) 100949.
[24] H. Okada, T.W. Mak, Pathways of apoptotic and non-apoptotic death in tumour cells, Nat. Rev. Cancer 4 (8) (2004) 592–603.
[25] X. Wang, P. Hua, C. He, M. Chen, Non-apoptotic cell death-based cancer therapy: molecular mechanism, pharmacological modulators, and nanomedicine, Acta Pharm. Sin. B 12 (9) (2022) 3567–3593.
[26] C. Liang, X. Zhang, M. Yang, X. Dong, Recent progress in ferroptosis inducers for cancer therapy, Adv. Mater. 31 (51) (2019) 1904197.
[27] J. Zhuang, R. Fan, W. Liao, R. Lin, A. Deng, T. Zhao, Y. Hai, H. Li, L. Tang, G. Wei, Organelle synergy unleashed: modulating mitochondrial-endoplasmic reticulum contacts with a self-assembled prodrug amplifies ferroptosis for innovative cancer therapy, Chem. Eng. J. 495 (2024) 153364.
[28] N. Kang, S. Son, S. Min, H. Hong, C. Kim, J. An, J.S. Kim, H. Kang, Stimuli-responsive ferroptosis for cancer therapy, Chem. Soc. Rev. 52 (12) (2023) 3955–3972.
[29] Y. Xie, W. Hou, X. Song, Y. Yu, J. Huang, X. Sun, R. Kang, D. Tang, Ferroptosis: process and function, Cell Death Differ. 23 (3) (2016) 369–379.
[30] D. Tang, X. Chen, R. Kang, G. Kroemer, Ferroptosis: molecular mechanisms and health implications, Cell Res. 31 (2) (2012) 107–125.
[31] X. Jiang, B.R. Stockwell, M. Conrad, Ferroptosis: mechanisms, biology and role in disease, Nat. Rev. Mol. Cell Biol. 22 (4) (2021) 266–282.
[32] C. Zhang, X. Liu, S. Jin, Y. Chen, R. Guo, Ferroptosis in cancer therapy: a novel approach to reversing drug resistance, Mol. Cancer 21 (1) (2022) 47.
[33] Y. Lai, N. Lu, A. Ouyang, Q. Zhang, P. Zhang, Ferroptosis promotes sonodynamic therapy: a platinum(ii)–indocyanine sonosensitizer, Chem. Sci. 13 (34) (2022) 9921–9926.
[34] L. Zhou, C. Dong, L. Ding, W. Feng, L. Yu, X. Cui, Y. Chen, Targeting ferroptosis synergistically sensitizes apoptotic sonodynamic anti-tumor nanotherapy, Nano Today 39 (2021) 101212.
[35] Q. Lei, W. Zhou, S. Gao, N. Sun, B. Wang, H. Yang, J. Wang, Y. Zhao, Q. Chen, J. Tian, L. Cai, F. Yan, Ultrasound-responsive metal-organic framework-based nanosystem for sonodynamic therapy/amplified ferroptosis/Ido-blockade osteosarcoma immunotherapy, Chem. Eng. J. 490 (2024) 151614.
[36] Z. Wang, Y. He, Y. An, G. Hu, Y. Tan, D. Xu, R. Liu, L. Yang, M. Li, Y. Cheng, L. Zheng, W. Liu, G. Liu, Z. Lu, Mitochondrion-specific organometallic sonosensitizer boosts synergistic sonodynamic therapy for augmented ferroptosis to trigger systemic immunity, Nano Today 57 (2024) 102369.
[37] D. Berillo, B. Mattiasson, I.Y. Galaev, H. Kirsebom, Formation of macroporous self-assembled hydrogels through cryogelation of Fmoc–Phe–Phe, J. Colloid Interface Sci. 368 (1) (2012) 226–230.
[38] H. Zhang, M. Jiang, W. Xing, R. Zhao, G. Li, Z. Zheng, Peptide-IR820 conjugate: a promising strategy for efficient vascular disruption and hypoxia induction in melanoma, ACS Appl. Mater. Interfaces 16 (31) (2024) 40641–40652.
[39] H. Zhang, L. Peng, W. Qin, D. Jia, R. Zhao, M. Jiang, M. Ji, L. Wang, G. Li, Z. Zheng, Enhanced chemotherapy and anti-metastasis with in situ nanosphere-to-nanofiber transition, Nano Today 54 (2024) 102122.
[40] H. Zhang, L. Peng, W. Qin, D. Jia, R. Zhao, M. Jiang, M. Ji, L. Wang, G. Li, Z. Zheng, Enhanced chemotherapy and anti-metastasis with in situ nanosphere-to-nanofiber transition, Nano Today 54 (2024) 102122.
[41] X. Meng, J. Wu, Z. Hu, X. Zheng, Z. Wang, Coordinating effect of ferroptosis and in situ disulfiram toxification for enhanced cancer therapy, Chem. Eng. J. 484 (2024) 149313.
[42] W. Xu, Y. Wang, G. Hou, J. Wang, T. Wang, J. Suo, A. Qian, Tumor microenvironment responsive hollow nanoplatform for triple amplification of oxidative stress to enhance cuproptosis-based synergistic cancer therapy, Adv. Healthcare Mater. 12 (13) (2023) 2202949.
[43] P. Zhu, Y. Chen, J. Shi, Piezocatalytic tumor therapy by ultrasound-triggered and BaTiO3-mediated piezoelectricity, Adv. Mater. 32 (29) (2020) 2001976.
[44] C. You, X. Li, D. Wang, H. Chen, L. Liang, Y. Chen, Y. Zhao, H. Xiang, Self-assembled aza-boron-dipyrromethene for ferroptosis-boosted sonodynamic therapy, Angew. Chem. Int. Ed. 61 (41) (2022) e202210174.
[45] J. Zhao, E. Bian, R. Zhang, T. Xu, Y. Nie, L. Wang, G. Jin, H. Xie, H. Xiang, Y. Chen, D. Wu, Self-assembled aza-boron-dipyrromethene-based H_2S prodrug for synergistic ferroptosis-enabled gas and sonodynamic tumor therapies, Adv. Sci. 11 (2024) 2309452.
[46] N. Sun, Q. Lei, M. Wu, S. Gao, Z. Yang, X. Lv, R. Wei, F. Yan, L. Cai, Metal-organic framework-mediated siRNA delivery and sonodynamic therapy for precisely triggering ferroptosis and augmenting ICD in osteosarcoma, Mater. Today Bio 26 (2024) 101053.
[47] Y. Yang, J. Huang, M. Liu, Y. Qiu, Q. Chen, T. Zhao, Z. Xiao, Y. Yang, Y. Jiang, Q. Huang, K. Ai, Emerging sonodynamic therapy-based nanomedicines for cancer immunotherapy, Adv. Sci. 10 (2) (2023) 2204365.